Electronic Supplementary Material (ESI) for Journal of Materials Chemistry A.

Flow Battery Electroanalysis 3: Online Kinetics Measurements Using Ultramicroelectrodes in Channel Flow

Electronic Supplementary Information

Becca Segel, Zachary Parr, Tejal V. Sawant, Carissa S. Yim, Dean M. Miller, Thomas J. Henry, and James R. McKone*
Department of Chemical and Petroleum Engineering
University of Pittsburgh
Pittsburgh, PA 15261

1 Materials and Methods

The experimental apparatus (Figure S1) was constructed using a commercial RFB stack (TDM LLC, fuelcellstore.com). The RFB stack included polymeric endplates, two copper coated current collectors, two graphite plates with interdigitated flow fields, two PTFE gaskets, two carbon felt squares 10 cm^2 in area, and a Nafion cation-exchnage membrane. A single set of battery hardware was used for all experiments without modifications except for routine cleaning and abrasive polishing of the current collectors.

To construct the RFB stack, an endplate was placed flat on a bench with the electrolyte inlets oriented at the top and the binding screws were inserted through the guide holes. Wooden toothpicks were used as guides to ensure the holes of the gaskets, membrane, and flow plates were properly aligned. The current collector was inserted into its socket on the inside of the endplate. Next, one of the graphite flow field plates was positioned so that electrolyte flow can enter the top left of the cell. A PTFE gasket was then placed on top of the graphite plate. Next, a piece of carbon felt was laid inside the square gasket and on top of the interdigitated flow field. The Nafion membrane was placed next on the carbon felt such that the edges overlapped with the PTFE gasket. Next, a second electrode, gasket, and graphite flow field were placed in reverse order, and the flow field was oriented so that electrolyte flow can enter in the top right of the stack and exit on the bottom left. Lastly, the second current collector and endplate were inserted and aligned with the binding screws. While the stack is held together by hand, washers and nuts were used to tighten the cell to finger tightness. The screws were then further tightened with a wrench in an alternating pattern to the maximum extent possible that did not result in any visible bowing of the endplates.

Next, the RFB stack was integrated into an electrolyte flow loop. The full apparatus consisted of the RFB stack, a peristaltic pump (MasterFlex), a three electrode half-cell (machined in house from PEEK), and two 10 mL reservoirs with compression fittings (Savillex) on each side. All components were connected using rubber peristaltic pump tubing (MasterFlex ChemDurance Bio) or clear polyethylene tubing (McMaster-Carr). Nylon Barb connectors (McMaster-Carr) were used to connect the rubber tubing to the clear plastic tubing and Nylon Luer adapters (McMaster-Carr) were used to connect peristaltic tubing into the three-electrode half-cell. Lastly, Nylon screw in Luer adapters(McMaster Carr) were inserted into the RFB stack to allow for connection of the clear plastic tubing.

The full apparatus was assembled by using a ring stand to hold the reservoirs in a vertical orientation, such that RFB electrolyte could enter the top and flow out the bottom. The reservoirs were further configured so that the inlet flow created a dripping action, which has the added benefit of preventing bubbles from accumulating in the flow lines. Clear plastic tubing ran from the first reservoir into the top left of RFB stack. The tubing was connected using the screw-in Luer adapters. Clear plastic tubing was also inserted into the opposite side of the RFB stack using a screw-in Luer adapter. Then the clear plastic tubing was further connected to peristaltic tubing using a barb connector. The barb connector was sealed with PTFE tape to prevent any leaks. Next, the peristaltic tubing was clamped into the rollers of the pump and further connected back into the clear plastic tubing using a barb connector lined with PTFE tape. Finally, the clear plastic tubing was run back into the starting reservoir.

The procedure above comprised assembly of the non-capacity limiting RFB half-cell. This was repeated for capacity-limiting half cell, except that the clear plastic tubing was also connected through the three-electrode analytical cell as schematized in Figure 2 of the main text using Luer and compression fittings. The half-cell was held in place using an additional arm connected to the same ring stand as with the reservoirs.

Next, electrodes were inserted into the analytical cell, which contains threaded holes for one working UME (Pt or C fiber, BASi), one counter-electrode (Alfa Aesar), and one reference electrode (Ag/AgCl, CH Instruments). Screws for each size of the respective electrodes were also machined in house. The screws were placed over each respective electrode and an O-ring was attached at the bottom of each electrode to prevent leaks. The electrodes were then screwed into their respective locations in the half-cell just until leak tight.

The next step was to make electrolyte for the cell. In a representative procedure, the non-capacity limiting electrolyte was made using a 50mL polypropylene centrifugation tube (Corning) to weigh 4.97g $FeCl_2 \cdot 4\,H_2O$ and 6.76g $FeCl_3 \cdot 6\,H_2O$ (Alfa Aesar). These salts were then solvated to 50 mL using a 2M HCl (aq). The 2M HCl solution was made diluting from a 12M HCl stock solution (Fisher Chemicals).

The tubes were sonicated and stirred as needed until the salts fully dissolved. The final concentration of the analyte was 0.5M Fe^{3+} and 0.5M Fe^{2+}. The capacity-limiting electrolyte was made in the same way using 9.94g $FeCl_2 \cdot 4\,H_2O$ and solvating to 50 mL total volume with 2 M HCl (aq). The final concentration of the catholyte was 1.0 M Fe^{2+}. Both sets of electrolytes were allowed to stand without stirring for at least 10 minutes prior to their use in experiments.

Next, the apparatus was cleaned of residues from prior experiments. To clean the apparatus, the plastic tubing was removed from the tops of both reservoirs and inserted into a beaker that contained deionized water. The peristaltic pump was then set to flow at 10 mL/min in the opposite direction from RFB operation. Water was flowed through the

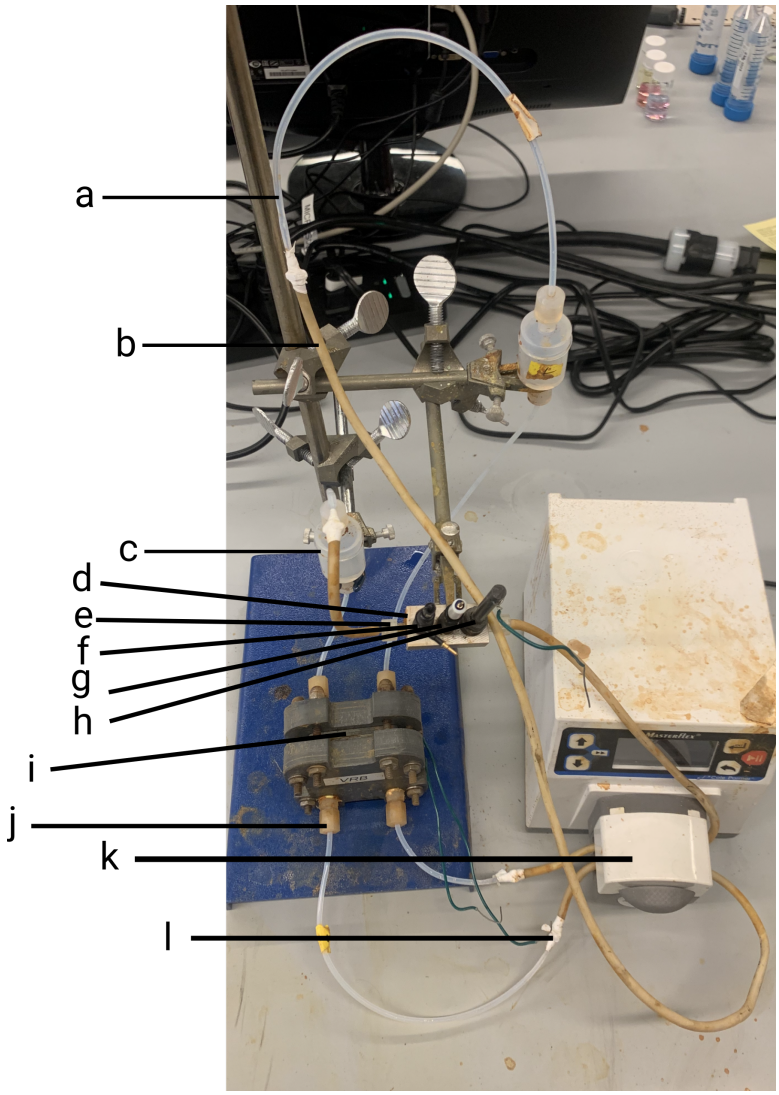

Figure S1: Photograph of the experimental apparatus with labels for key components described in the Materials and Methods section. The labels are as follows: (a) clear polyethylene tubing; (b) MasterFlex ChemDurance Bio peristaltic pump tubing; (c)Savillex reservoir; (d) PEEK three electrode cell; (e) Nylon Luer Adapter; (f) UME; (g) graphite counter electrode; (h) Ag/AgCl reference electrode; (i) Flex Stak FB cell; (j) Nylon Screw in Luer Adapter; (k) Masterflex peristaltic pump; and (l) Nylon barb connector. Note that in the RFB cell, the electrolyte in the tubing entering the cell on the back right actually exits from the front left, because of the interdigitated flow field. The electrolyte in the tubing entering the cell on the back left exits from the front right.

apparatus until both reservoirs contained ∼1 mL of water—note that this corresponds to 2–3 mL of water total when including the internal volumes of the RFB, analytical cell, and tubing. The pump was next paused so the plastic tubing could be reinserted into the tops of the reservoirs. The pump direction was then reversed and allowed to flow for 15 minutes before the water was drained from the apparatus and into a waste beaker.

Next, the working electrode was removed from the three electrode cell to be prepared via a series of polishing and pretreatment steps. A carbon fiber UME was polished by placing a piece of grinding paper inside a plastic Petri dish. A small quantity (approximately 0.25 mL by volume) of alumina powder with a 1-micron grit size was placed onto the grinding paper and wetted with water to generate a slurry of a similar consistency to cream or very thin acrylic paint. The electrode was held level with the bench top and polished in a circular motion via twenty rotations in both the clockwise and counterclockwise directions on the grinding paper. The electrode was then sonicated for 30 seconds to remove excess alumina powder. This process was then repeated using both 0.3- and 0.05-micron alumina powder. The entirety of this process was repeated for all UME working electrodes.

Carbon fiber UMEs were further pretreated by sonicating in pre-purified isopropanol, as reported previously.[1,2] In a representative procedure, a suspension containing 3.3 g of activated carbon (Alfa Aesar) and 9 mL of isopropanol(Alfa Aesar) was stirred for 5 minutes and then sonicated for 10 minutes. The mixture was then left to stand in air for 30 minutes. After 25 minutes, the working electrode of interest was polished as described above. The electrode was then submersed into the carbon slurry for 10 minutes. The electrode was finally rinsed and sonicated in deionized water for 30 seconds. Carbon fiber UMEs left in this condition as pristine or non-oxidized carbon in the main text.

To prepare oxidized carbon fiber UMEs, the electrodes were further placed into a separate single-chamber electrochemical cell comprising a 20 mL scintillation vial containing 0.5M H_2SO_4, a graphite counter electrode, and a Ag/AgCl reference electrode. The electrode was then cycled at 200 mV/sec from -0.25 to 1.5V vs. Ag/AgCl for 100 cycles and then 0.25 to 1.7V vs. Ag/AgCl for 20 cycles. Upon removal and rinsing with deionized water, electrodes were used immediately for analytical experiments.

Final assembly comprised filling the analytical apparatus with electrolyte and initiating charge–discharge and voltammetry experiments in the RFB and analytical cell, respectively. On the the capacity limiting side of the RFB, 3.5 mL of Fe^{2+} electrolyte was pumped into the apparatus at 10 mL/min. The volume was gauged by monitoring the negative volume displacement in a 15 mL polypropylene centrifugation tube. On the non-capacity limiting side of the apparatus, 12.5 mL of 0.5M $Fe^{3+/2+}$ electrolyte was pumped in at 10 mL/min while monitoring in the same fashion. Note that this total volume was the maximum that could be used while maintaining a modest headspace in the reservoirs to capture air bubbles.

Next, a potentiostat (Gamry, Reference 600) was connected to the current collectors of the RFB in a two-electrode configuration. A second potentiostat (of the same design) was connected to the analytical cell in a 3-electrode configuration. The potentiostat connected to the RFB was configured to run cyclic charge–discharge experiment using a constant current of $\pm$0.2 A. Half cycles were set to terminate after 2000 s had elapsed or the applied potential reached a limit of $\pm$0.6 V. The battery was cycled 5 times with a 1 s sample period.

The potentiostat connected to the analytical cell was configured to run cyclic voltammetry experiments continuously alongside battery charge–discharge over a potential range from 0.1 to 0.9 V vs. Ag/AgCl at 20 mV/s without iR compensation. In a representative run, 160 CVs were performed over a total of 2.7 hours, which was the total time required to charge/discharge the flow battery over 5 cycles. A total of 5 replicates were completed for each type of UME, for a total of 15 experimental runs. The data in the main text comprise representative results, which were chosen by avoiding data corresponding to the highest or lowest values of reaction rate constant, battery capacity, charge–discharge time. Complete datasets for all experimental runs have been assembled in the following section.

S2 Comprehensive Charge–Discharge and Voltammetry Data

Figures S2 and S3 collect cell voltage, reaction rate constant, and state of charge data from each of 15 RFB charge–discharge experiments, analogous to the results shown in Figures 4 and 6 in the main text. The relatively high level of run-to-run variability is notable, and we speculate that it is representative of what can be expected from an un-optimized flow battery system in an academic laboratory setting, where experimental runs giving rise to poor overpotential performance or erratic reaction kinetics would often be discarded as failed experiments. We have instead included all data and drawn conclusions based on aggregate observations and statistical treatments of the full set.

Over 15 experimental runs, the total time to cycle the battery 5 times varied rather widely, from approximately 2.5 to 4 hours. This difference is attributable to variability in the volume of capacity-limiting electrolyte that was used (we targeted 3.5 mL, but the total likely varied between 3 and 4 mL) and variations in the total capacity that was accessed in each run (as depicted in the state of charge data in Figure S3). Another notable observation was the hysteresis between

charge and discharge voltages varied considerably, from $\pm$100 to $\pm$250 mV at the midpoint of the charge–discharge plateaus. We tentatively attribute these differences to variability in the electroactive surface area of the carbon cloth electrodes, and specifically to the tendency of the carbon cloth never to become fully wetted by the electrolyte in some experimental runs. Another possibility is that the copper current collectors were found to corrode over time due to incidental contact with the $Fe^{3+/2+}$/HCl electrolyte during cell disassembly, which may have resulted in increased series resistance for runs that were completed between successive abrasive polishing procedures.

We also note one experimental run in particular (fourth row in the second column of Figure S2) where the open-circuit potential data followed an unusual sinusoidal pattern rather than the expected roughly triangular shape. This behavior is consistent with the presence of a significant fraction of unwetted battery electrode accompanied by a bypass flow in the RFB (where some unreacted electrolyte is allowed to flow directly from the inlet to outlet), which limits the ability of the battery to obtain a fully charged or discharged state even if the cell voltage reaches the cutoff limits.

Electron-transfer kinetics data also exhibited considerable variability, but several notable trends are readily observable. In four out of five cases rate constants increase over time for Pt UMEs. By contrast, carbon electrodes gave smaller and less consistent changes in rate constant (as further reflected in the statistical analysis in main text Figure 6). One trial using oxidized carbon UME (third row, third column in Figure S3) yielded erratic kinetics data that are directly attributable to a degraded electrical connection to the UME caused by moving the potentiostat during the experiment. A majority of experimental runs (13) gave clear evidence of a correlation between state of charge and reaction rate constant. In most cases the correlation was positive (faster kinetics at higher state of charge), but in other cases the correlation was either negative or the rate constant appeared to increase upon approaching both the minimum and the maximum state of charge. Ultimately these cycle-to-cycle trends are relatively small compared to the variability in rate constant across experimental runs, so we are reluctant to draw concrete conclusions beyond the discussion in the main text. However, with improved measurement precision it should be possible to use these types of measurements to test hypotheses regarding reaction mechanisms (i.e., those involving positive or negative reaction orders in reactant/product concentration) for charge transfer in RFB active materials.

S3 Compiled Literature Values of Electron Transfer Rate Constant

To illustrate the need to perform high-quality analytical measurements, Table S1 presents a representative set of heterogeneous electron transfer rate constants reported in the literature for four popular RFB electrolytes at various types of carbon electrodes. These data were collected from some studies that were directed at RFB operation and others that were directed at the fundamental chemistry and physics of interfacial electron-transfer. Accordingly, only a subset of these values include accompanying measurements of RFB figures of merit, which in turn makes it challenging to contextualize differences in kinetics in terms of device-level performance. The large spread in these data clearly indicates that electron-transfer processes remain poorly understood even in well-established RFB active materials. While some of this ambiguity results from the use of different carbon materials and experimental conditions, differences in interfacial electron transfer kinetics of up to several orders of magnitude have been reported even while holding these constant.

S4 Impact of Varying the Charge Transfer Coefficient

A charge transfer coefficient, α, of 0.5 was used in our Butler-Volmer fits in this study. In practice, electron transfer reactions obey Butler-Volmer kinetics if they involve no coupled chemical reactions (including adsorption-desorption events for catalytic reactions) or if coupled reactions are sufficiently fast so that charge-transfer is rate determining. This generally leads to α values that fall in a narrow range relatively close to 0.5. To further improve accuracy in determining k^0_{eff} , α could be included in the least-squares regression, but doing so without constraining its value could lead to unphysical results where extreme values of α generate the best fit to data that are heavily mass-transfer limited. Thus, we recommend applying constraints, such as $0.2 < \alpha < 0.8$ when using the shrinking overpotential method to fit kinetics data. If this results in generally poor fits, another kinetic model should be considered.

To further illustrate the relatively modest impact of α values that deviate from 0.5 on k^0_{eff} results, Figure S4 compiles simulated CV data and shrinking overpotential fits for $k^0 = 10^{-4}$ cm/s and 50% state of charge while iteratively decreasing α from 0.5 to 0.1. The shrinking overpotential fits were then carried out while constraining $\alpha = 0.5$, as in the main text, to observe the systematic error this would introduce. Note that increasing α from 0.5 to 0.9 would have the same impact on the fits because the J vs. η data are symmetric about $\eta = 0$. With an alpha value of 0.5, k^0_{fit} clearly asymptotes at the true k^0 value of 10^{-4} cm/s. As α decreases, k^0_{fit} overshoots the true k^0 (clearest in the detail Panel S4c) before decreasing again toward the true k^0 as η approaches zero. These data show that, if we take the maximum of k^0_{fit} as an estimate of k^0_{eff} , the systematic error approaches the relative uncertainty we extracted from

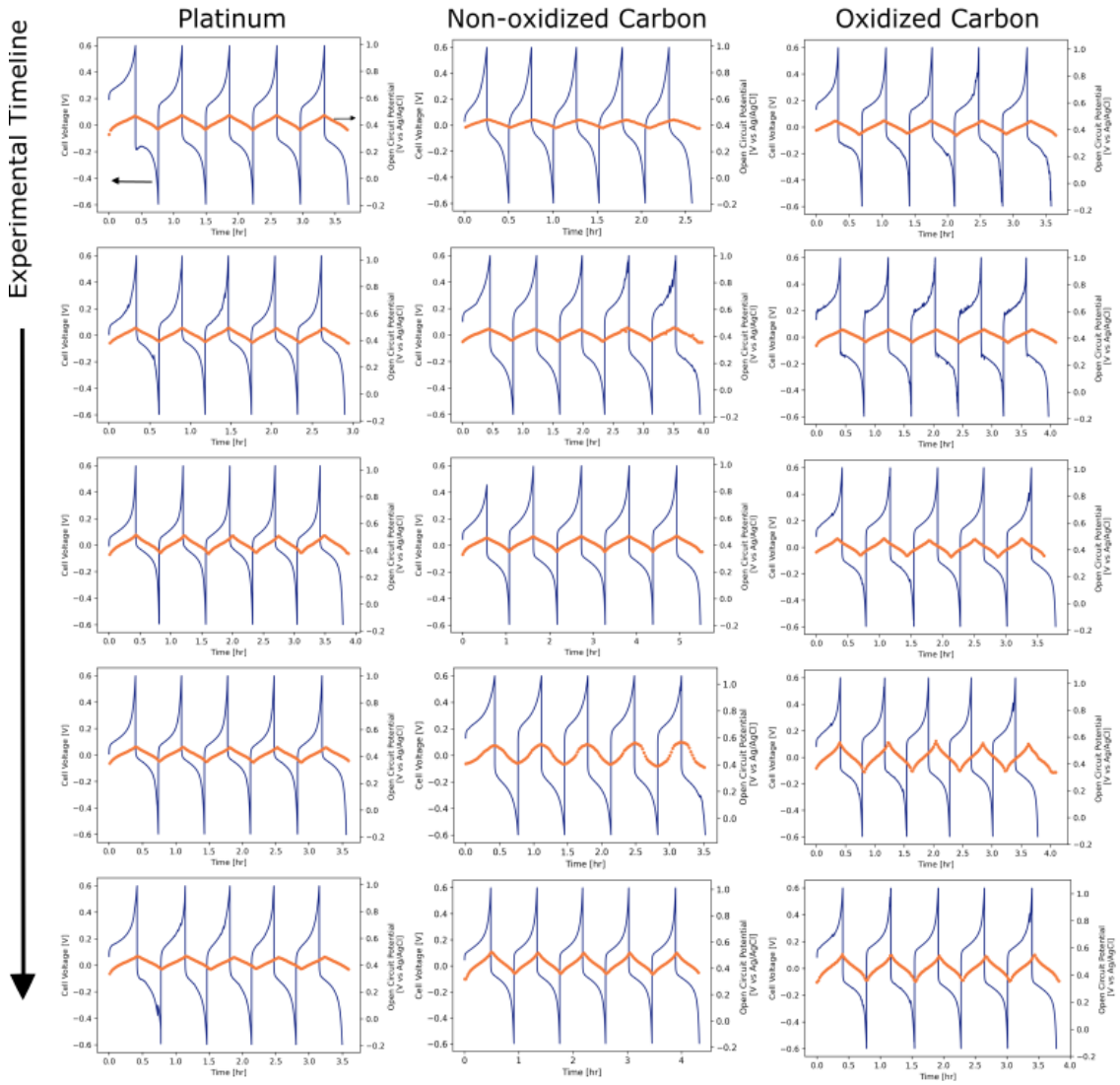

Figure S2: Cell voltage and open-circuit voltage vs. time from all 15 experiments runs in the RFB and analytical cell, respectively.

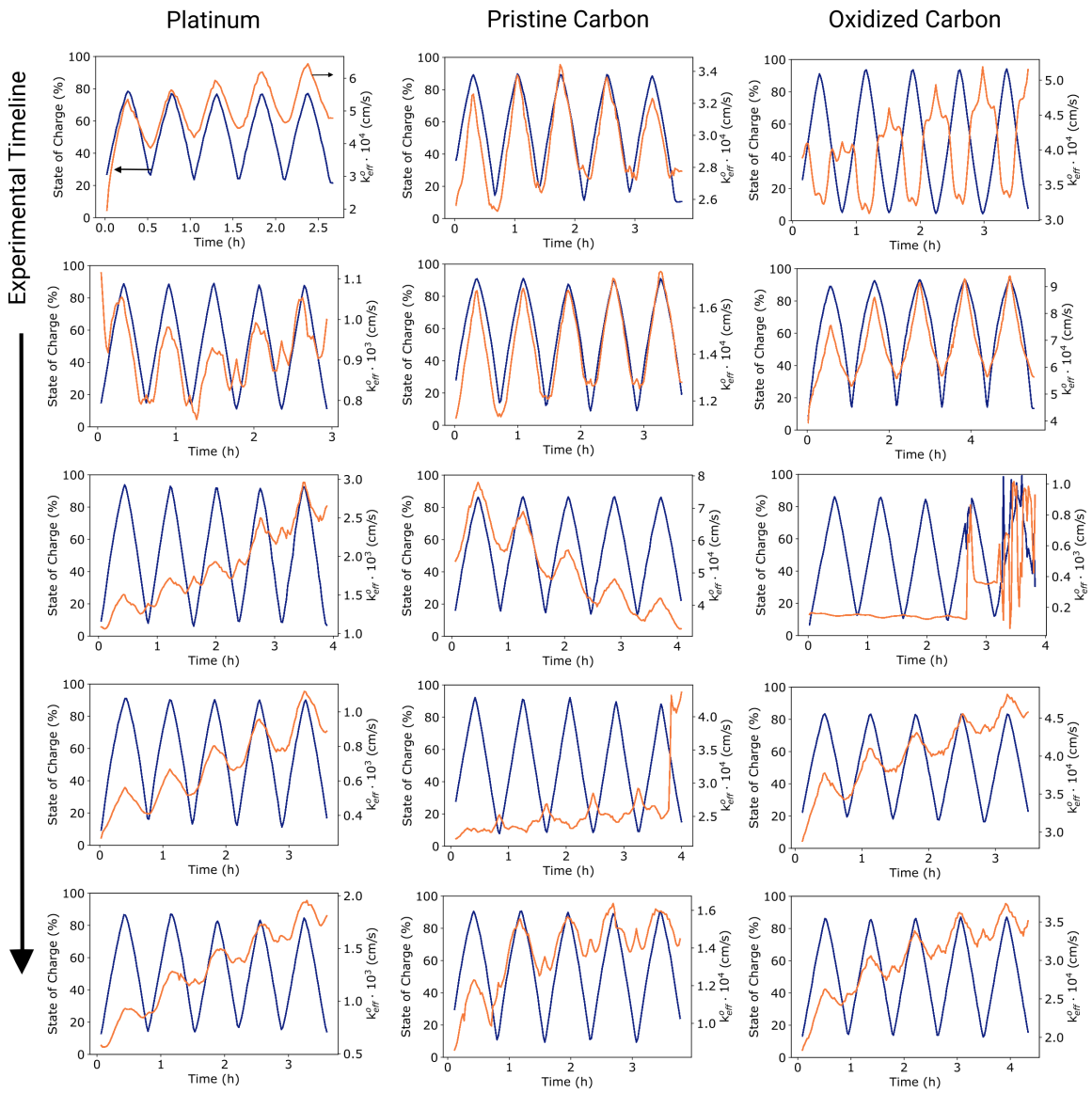

Figure S3: State of charge and effective reaction rate constants vs. time for each of 15 experimental trials. Columns denote UME working electrode identity and rows are organized from top to bottom in the order the experiments were completed.

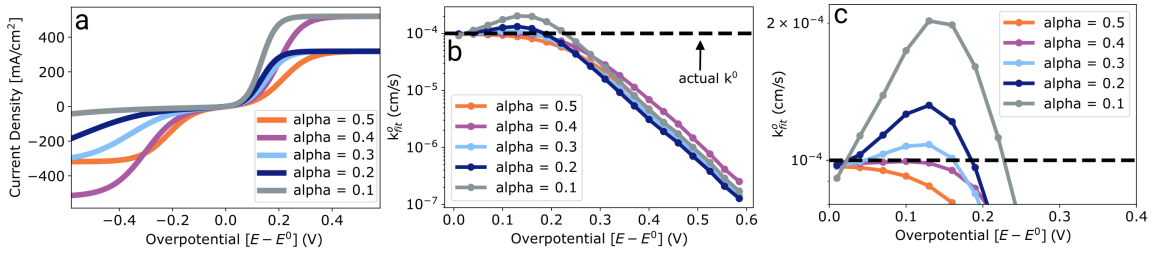

Figure S4: Simulated J–η data (a) and shrinking overpotential results (b,c) while systematically varying the charge transfer coefficient from 0.5 to 0.1 in 0.1 unit increments.

replicate measurements (see main text Figure 6) only for $\alpha \leq 0.1$. Moreover, the non-monotonic shape of the k^0_{fit} vs. η response may be used as an additional qualitative indicator that α may be wrong or that the Butler-Volmer equation may not be the right kinetic model.

S5 Defining an Upper Bound of Measurable Rate Constants

Figure S4 compiles additional shrinking overpotential fits to simulated voltammetry data over the range in k^0 values from 10^{-5} to 10^{-2} cm/s. Note that the simulated data featured limiting current densities $J_{\mathrm{lim}} = \pm 0.3$ A/cm^2. These data clearly show that the k^0_{fit} values asymptotically converge on the true value of k^0 up to $k^0 = 10^{-4}$ cm/s, but not at larger values of k^0. This is a consequence of the fact that there simply exists no potential range over which the current-overpotential behavior is dominated by reaction kinetics. Conveniently, the shrinking overpotential method yields a very clear visual cue for this behavior, which is the tendency of the k^0_{fit} values not to fully level off even over very small overpotential ranges.

Techniques like rotating-disk electrode voltammetry and Koutecký-Levich analysis can also be used to extract transport-free kinetic current densities from voltammetry data that include significant contributions from mass transfer. In practice, this extends the upper bound of k^0 values that can be accurately measured by perhaps one order of magnitude (i.e., up to the range where J_{lim} is comparable or slightly smaller than J_0). But similar increases in experimentally accessible k^0 values can also be obtained by further increasing convection in a channel-flow system. Indeed, prior work using channel-flow configurations for electroanalysis have shown that extremely fast rates of mass transfer can be obtained.[18] Thus, we conclude that channel-flow techniques like those presented here are especially suitable for kinetics measurements in RFBs where flowing electrolytes are already the norm.

Table S1: Compiled kinetics data for aqueous RFB redox couples at various types of carbon electrodes

redox couple	electrode material	rate constant, k^0 (cm/s)	measurement technique	supporting electrolyte	concentration of active species	Ref.
$Fe^{3+/2+}$	glassy carbon	7.3 x 10^{-5}	RDE	2 M H_2SO_4	1 M	Yang[3]
	glassy carbon	2.3 x 10^{-3}	RDE	0.2 M $HClO_4$	5 mM	McDermott[4]
	glassy carbon	1 x 10^{-3}	RDE	0.3 M HCl	1 mM	Stulikova[5]
	pyrolytic graphite	5.2 x 10^{-4}	RDE	4 M HCl	0.1 M	Ateya[6]
	pyrolytic graphite	1.0 x 10^{-3}	CV	1.5 M HCl	1 M	Hollax[7]
$V^{3+/2+}$	glassy carbon	1.0 x 10^{-6}	potentiostatic polarization	4.2 M H_2SO_4	1.6 M	Oriji[8]
	glassy carbon	1.4 x 10^{-4}	EIS	4.5 M H_2SO_4	1.5 M	Bourke[9]
	electrochemically activated graphite	1.1 x 10^{-6}	CV	2 M H_2SO_4	2 M	Liu[10]
	carbon felt	1.4 x 10^{-6}	LSV	0.1 M H_2SO_4	150 mM	Li[11]
	carbon felt	1.5 x 10^{-5}	CV	1 M H_2SO_4	50 mM	Agar[12]
	carbon paper	1.1 x 10^{-3}	CV	1 M H_2SO_4	50 mM	Wu[13]
VO_2^+/VO^{2+}	glassy carbon	2.2 x 10^{-6}	potentiostatic polarization	4.2 M H_2SO_4	1.6 M	Oriji[8]
	glassy carbon	4.5 x 10^{-5}	EIS	4.5 M H_2SO_4	1.5 M	Bourke[9]
	electrochemically activated graphite	8.2 x 10^{-4}	CV	2 M H_2SO_4	2 M	Liu[10]
	carbon nanotubes	1.8 x 10^{-6}	CV	1 M H_2SO_4	100 mM	Friedl[14]
	carbon paper	1.0 x 10^{-3}	CV	1 M H_2SO_4	50 mM	Wu[13]
	carbon–polymer composite	8.5 x 10^{-4}	CV	1 M H_2SO_4	50 mM	Yamamura[15]
AQDS/$AQDSH_2$	glassy carbon	7.2 x 10^{-3}	RDE	1 M H_2SO_4	1 mM	Huskinson[16]
	glassy carbon	1.5 x 10^{-4}	RDE	1 M H_2SO_4	1 mM	Yang[3]
	glassy carbon	4.8 x 10^{-4}	CV	1 M H_2SO_4	10 mM	Lantz[17]
	glassy carbon	1.5 x 10^{-4}	RDE	2 M H_2SO_4	1 M	Yang[3]

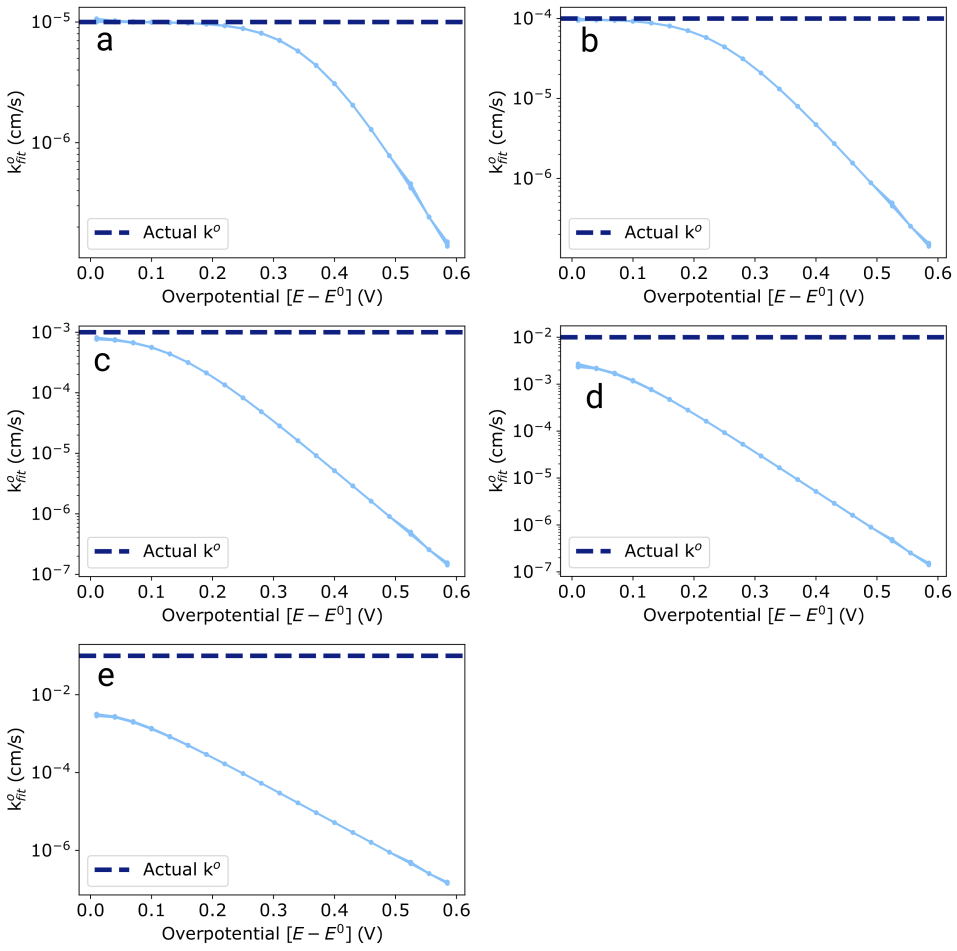

Figure S5: Simulations for varying kinetic activity with respect to overpotential, extracted by the shrinking overpotential method

References

[1] T. V. Sawant and J. R. McKone, *Journal of Physical Chemistry C*, 2019, **123**, 144–152.

[2] S. Ranganathan, T. C. Kuo and R. L. McCreery, *Analytical Chemistry*, 1999, **71**, 3574–3580.

[3] B. Yang, A. Murali, A. Nirmalchandar, B. Jayathilake, G. K. S. Prakash and S. R. Narayanan, *Journal of The Electrochemical Society*, 2020, **167**, 060520.

[4] C. A. McDermott, K. R. Kneten and R. L. McCreery, *Journal of The Electrochemical Society*, 1993, **140**, 2593.

[5] M. Štulíková and F. Vydra, *Journal of Electroanalytical Chemistry and Interfacial Electrochemistry*, 1972, **38**, 349–357.

[6] B. G. Ateya and L. G. Austin, *Journal of The Electrochemical Society*, 1973, **120**, 1216.

[7] E. Hollax and D. S. Cheng, *Carbon*, 1985, **23**, 655–664.

[8] G. Oriji, Y. Katayama and T. Miura, *Journal of Power Sources*, 2005, **139**, 321–324.

[9] A. Bourke, M. A. Miller, R. P. Lynch, X. Gao, J. Landon, J. S. Wainright, R. F. Savinell and D. N. Buckley, *Journal of The Electrochemical Society*, 2016, **163**, A5097–A5105.

[10] H. Liu, L. Yang, Q. Xu and C. Yan, *RSC Advances*, 2014, **4**, 55666–55670.

[11] Y. Li, J. Parrondo, S. Sankarasubramanian and V. Ramani, *Journal of Physical Chemistry C*, 2019, **123**, 6370–6378.

[12] E. Agar, C. R. Dennison, K. W. Knehr and E. C. Kumbur, *Journal of Power Sources*, 2013, **225**, 89–94.

[13] X. W. Wu, T. Yamamura, S. Ohta, Q. X. Zhang, F. C. Lv, C. M. Liu, K. Shirasaki, I. Satoh, T. Shikama, D. Lu and S. Q. Liu, *Journal of Applied Electrochemistry*, 2011, **41**, 1183–1190.

[14] J. Friedl and U. Stimming, *Electrochimica Acta*, 2017, **227**, 235–245.

[15] T. Yamamura, N. Watanabe, T. Yano and Y. Shiokawa, *Journal of The Electrochemical Society*, 2005, **152**, A830.

[16] B. Huskinson, M. P. Marshak, C. Suh, S. Er, M. R. Gerhardt, C. J. Galvin, X. Chen, A. Aspuru-Guzik, R. G. Gordon and M. J. Aziz, *Nature*, 2014, **505**, 195–198.

[17] A. W. Lantz, S. A. Shavalier, W. Schroeder and P. G. Rasmussen, *ACS Applied Energy Materials*, 2019, **2**, 7893–7902.

[18] N. V. Rees, J. A. Alden, R. A. W. Dryfe, B. A. Coles and R. G. Compton, *J. Phys. Chem*, 1995, **99**, 14813–14818.